Chemical Engineering Journal 159 (2010) 182–189

Contents lists available at ScienceDirect

Chemical Engineering Journal

journal homepage: www.elsevier.com/locate/cej

Development of a single stage heat integrated water–gas shift reactor for fuel processing

H.A.J. van Dijk*, J. Boon, R.N. Nyqvist, R.W. van den Brink

Energy Research Centre of the Netherlands (ECN), P.O. Box 1, 1755 ZG Petten, The Netherlands

ARTICLE INFO

Article history:
Received 27 November 2009
Received in revised form 19 February 2010
Accepted 23 February 2010

Keywords:
Water–gas shift
Kinetics
Heat integration
Isothermal adiabatic reactor
Reactor design
Fuel processing

ABSTRACT

Compacting of the water–gas shift (WGS) section within a fuel processor for fuel cell based power generation by means of heat integration is presented. The concept of isothermal adiabatic operation is demonstrated. Isothermal adiabatic operation is achieved by dissipating the reaction heat throughout the catalyst support structure by means of thermal conduction. Thus the reactor overall behaves adiabatically, while the catalyst bed is nearly isothermal, while no active heat exchange with a second medium is applied. The concept allows for a much lower feed temperature. Accordingly, the conventional double staged WGS reactors with intermediate heat exchange can be replaced with a single WGS reactor. Two reactor designs, based on aluminum metal foam and aluminum metal monolith were evaluated. For the design of the isothermal adiabatic reactor, the intrinsic kinetics for a noble-metal WGS catalyst was measured and a power law rate equation was obtained. Isothermal adiabatic operation was approached for the foam, mainly hampered by a troublesome catalyst coating. The monolith allows for a simpler reactor design and its performance agreed well with model predictions. Simulations of the process dynamics further indicate superior performance of the isothermal adiabatic concept compared to the adiabatic concept. This would allow a much simpler control philosophy for the WGS section in a fuel processor.

1. Introduction

Small-scale electricity production on board of cars, trucks, and ships as well as at remote locations lacking electricity and fuel grids are viable niche markets for the introduction of polymer electrolyte membrane fuel cells (PEMFC). Such stand-alone electricity production units either rely on bottled H_2 or on the processing of a hydrocarbon fuel into a H_2-rich product. Since liquid fuels have much larger volumetric energy contents than bottled H_2, on-site fuel processing yields compacter systems. Two basic layouts for the fuel processor can be envisioned, one being a generator of high purity H_2 and the other of a H_2-rich reformate that still contains CO_2, CH_4, N_2 and steam but has <10 ppm CO. Fuel desulphurization and fuel conversion by partial oxidation, steam reforming or autothermal reforming are the first steps. Most logistic fuels require high-temperature conversion that leads to significant CO formation, exceptions being, e.g. methanol and dimethylether [1]. Both steam reforming and autothermal reforming at 750–800 °C result in CO levels of around 8 vol.% of the reformat. Accordingly, subsequent CO cleanup is necessary. The reformate producing fuel processor relies on the water–gas shift (WGS) reaction in combination with either a CO preferential oxidation (PrO*x*) reaction or a methanation reaction as final CO polishing step. The high purity H_2 producing fuel processor on the other hand relies on the WGS reaction and a H_2 separation step being either pressure swing adsorption (PSA) or a H_2-selective Pd-based membrane [2,3].

For both types of fuel processors, the WGS reaction is an essential step to reduce the CO content while simultaneously increasing the H_2 content. Within the fuel processor, noble-metal based WGS catalysts are preferred over conventional low-temperature CuZn-based catalysts and high-temperature FeCr-based catalysts. In contrast to these conventional base-metal catalysts, noble-metal catalysts do not require pre-reduction and can safely be exposed to air during the frequent start-up and shut-down procedures inevitably encountered in fuel processors [4]. Several commercial WGS catalysts utilizing platinum group metals and designed for fuel processing related to fuel cells are available on the market today.

Compactness of the WGS section and ease of operation are important aspects for small-scale fuel processors. For all chemical reactors encountered within the fuel processor, proper heat management is key for efficient use of catalyst. The conventional configuration of a WGS section within a fuel processor makes use of adiabatic reactors, i.e. without active cooling to a second medium. Because of the temperature rise associated with the exothermal

* Corresponding author at: Energy Research Centre of the Netherlands (ECN), Clean Fossil Fuels, Westerduinweg 3, P.O. Box 1, 1755 ZG Petten, Noord Holland, The Netherlands. Tel.: +31 224 564259; fax: +31 224 568489.
E-mail addresses: h.vandijk@ecn.nl (H.A.J. van Dijk), boon@ecn.nl (J. Boon), nyqvist@ecn.nl (R.N. Nyqvist), vandenbrink@ecn.nl (R.W. van den Brink).

1385-8947/$ – see front matter © 2010 Elsevier B.V. All rights reserved.
doi:10.1016/j.cej.2010.02.046

Nomenclature

A_{cross}	cross-sectional area for the flow field (m^2)
$c_{p,mol,g}$	molar heat capacity of the gas ($J\,mol^{-1}\,K^{-1}$)
$c_{p,s}$	heat capacity of the solid ($J\,kg^{-1}\,K^{-1}$)
E_a	activation energy ($J\,mol^{-1}$)
F_m	molar flow rate ($mol\,s^{-1}$)
F_v	volume flow rate ($Nl\,min^{-1}$)
GHSV	gas hourly space velocity (h^{-1})
$\Delta_r H_{WGS}$	heat of the WGS reaction ($J\,mol^{-1}$)
k	reaction rate constant (dependent)
k^0	pre-exponential factor (dependent)
K_{eq}	equilibrium constant for the WGS reaction
l	length of the catalyst bed (m)
n_i	reaction order for component i
P	total pressure (kPa)
p_i	partial pressure of component i (kPa)
R	gas constant ($J\,mol^{-1}\,K^{-1}$)
R_{WGS}	WGS reaction rate ($mol\,kg_{cat}^{-1}\,s^{-1}$)
R_{WGS}^{in}	WGS reaction rate at reactor entrance conditions ($mol\,kg_{cat}^{-1}\,s^{-1}$)
T	temperature (K)
T_{ref}	reference temperature for reparameterization (K)
T^{in}	temperature at reactor entrance (K)
k_{ref}	pre-exponential factor at reference conditions (dependent)
W_{cat}	amount of catalyst in the reactor (kg)
WHSV	weight hourly space velocity ($m^3\,kg^{-1}\,h^{-1}$)
V_R	volume of the reactor (m^3)
W_s	total amount of solid in the reactor (kg)
x	axial reactor coordinate (m)
x_i	molar fraction of component i on dry basis
X_{co}	CO conversion
Z	reduced temperature factor (K^{-1})
β	approach to equilibrium
λ_{eff}	effective thermal conductivity ($W\,m^{-1}\,K^{-1}$)
ρ_{gas}^{in}	density of the gas at reactor entrance conditions ($mol\,m^{-3}$)
ν_i	reaction stoichiometry for component i

Dimensionless numbers

Pe_{th}	thermal Peclet number $= (F_m \cdot c_{p,mol,g} \cdot l)/(A_{cross} \cdot \lambda_{eff})$
Le	Lewis number $= (W_{cat} \cdot c_{p,s})/(V_R \cdot \rho_{gas}^{in} \cdot c_{p,mol,g})$
Da_{th}	thermal Damkhöler number $= (W_{cat} \cdot {}_r H_{WGS} \cdot R_{WGS}^{in})/(F_m \cdot c_{p,mol,g} \cdot T^{in})$
τ	dimensionless time $= t \cdot ((F_m)/(\rho_{gas}^{in} \cdot V_R))$
T^*	dimensionless temperature $= T/T^{in}$
R_{WGS}^*	dimensionless reaction rate $= R_{WGS}/R_{WGS}^{in}$
z	dimensionless bed length $= x/l$

WGS reaction, typically two adiabatic reactors with intermediate heat exchange are required to reach sufficiently low CO levels [5]. Compacting by applying active heat exchange can be efficiently realized in micro-structured reactors [6,7]. Their design allows for isothermal operation or operation with a declining temperature gradient. An important parameter in these micro-structured reactors is the thermal conductivity of the solid phase. For isothermal operation, the thermal conductivity should be high, while this is not necessarily true in case a declining temperature gradient is desired. A high thermal conductivity of the solid phase would lead to an unwanted flattening of the desired temperature gradient in the direction of the flows. To reach the optimal declining temperature profile, careful tuning of the thermal conductivity of the solid phase is required [8]. Opposed to micro-structured reactors, Groppi showed that radial isothermal operation of a cooled honeycomb monolith reactor is enhanced by increasing the thermal conductivity of the monolith [9,10]. Hot-spot formation for the highly exothermal CO oxidation reaction was suppressed by going from cordierite to copper and assuring good thermal contact between the monolith and the cooled reactor wall.

This paper describes the development of a heat integrated WGS reactor that does not rely on active heat exchange with a fluid. Instead, the reaction heat is distributed throughout the catalyst mass by means of conduction of the catalyst support. Accordingly, the catalyst structure within the reactor becomes nearly isothermal. Because no active heat exchange is applied, the overall reactor operates under adiabatic boundary conditions. Nevertheless, some heat loss to the environment will occur. This reactor concept is called isothermal adiabatic operation. For reactor design, the intrinsic kinetics of the WGS reaction over a commercial noble-metal based catalyst was determined. The catalyst used is the Protonics™ W-type from Umicore. It was wash coated on two types of high conductivity catalyst supports: an aluminum metal foam and an aluminum metal monolith. The designed reactors were validated experimentally and the favorable process dynamics of the isothermal adiabatic reactor concept over the adiabatic operation is demonstrated via modeling.

2. WGS kinetics

2.1. Experimental apparatus

The intrinsic kinetics of water–gas shift reaction for the Protonics™ W-type catalyst from Umicore is measured on a high-throughput parallel flow test-rig containing six reactors. All gaseous reactants are fed via mass flow controllers. Steam is added using a Bronkhorst CEM system and the resulting feed gas is distributed over the reactors via high-temperature mass flow controllers. A bypass having a mass flow meter is included to assure an accurate mass balance. Downstream the steam addition, all components are placed in a furnace and maintained at a temperature of 363 K to prevent condensation. The quartz reactors have an internal diameter of 4 mm and are placed in a silver oven block to ensure isothermal operation. A thermocouple is placed directly downstream the catalyst bed. Depending on the reaction temperature, the catalysts are diluted on μm powder scale with inert α-alumina (AKP-15, Sumitomo Chemical, Japan), before the particle-size fraction of 0.212–0.300 mm was made. Additionally, the catalyst bed was diluted with inert α-alumina particles in the same size distribution to ensure intrinsic kinetics for all measurements. It has been checked that the AKP-15 alumina used had no effect on catalyst activity and stability.

2.2. Experimental methods

A design of experiments approach was used to set the experimental conditions [11]. The parameters were the reaction temperature and the concentrations of H_2O, CO, CO_2 and H_2. At every temperature, the concentrations of all components were varied according to a 4^2 design including a centre point, an orthogonal star and a face-centered star. Accordingly, five experimental points are obtained for each parameter describing the main effect. This allows for an easy check of the consistency of the experimental results. The central point was similar for all temperatures, i.e. 20 vol.% H_2O, 6 vol.% CO, 10 vol.% CO_2, 25 vol.% H_2, balance N_2. Within the design all concentrations were varied by a factor of typically 20 (=max/min), except for H_2O which was varied by a factor

Table 1
Extremes for the concentrations (vol.%) of the reactants and products within the experimental design space for the kinetic experiments.

	H_2O		CO		CO_2		H_2	
	Min	Max	Min	Max	Min	Max	Min	Max
200 °C	1.8	27	0.45	18	1.5	30	2.0	40
250 °C	2.0	27	0.45	17	1.5	30	2.0	50
300 °C	4.0	27	0.45	17	1.5	30	1.8	40
350 °C	5.0	27	1.2	15	1.5	30	2.5	50
400 °C	8.0	27	1.5	17	1.5	30	2.5	50

of typically 10, see Table 1. Since multiple reactors are available in the test-rig and the flow per reactor is variable, the GHSV is varied by a factor of 10 for every experimental setting.

Measurements were performed at 1.5 bar absolute pressure. The temperature was varied from 473 K to 673 K at 50 K intervals. At every temperature, fresh catalyst was used. For every run, the catalyst was conditioned for 60 h at the settings of the central point. Then the kinetic experiments were conducted over a period of 20 h and the centre point was measured again for 10 h. The catalyst performance at the conditions of the centre point varied <5% relative before and after the kinetic experiments. It was numerically verified that the experiments were performed in an isothermal reactor in the absence of inter- and intra-particle heat and mass transfer resistances [12].

The dried product gas (Permapure drier) is analyzed by GC for CO, CO_2, H_2 and CH_4. Methane formation was negligible at <10 ppm at all conditions. In general, the C-balance was accurate within 2%. The CO conversion is calculated using the measured dry molar fraction for either CO or CO_2 according to Eqs. (1a) and (1b). Eq. (1a) was used when $x_{CO}^{in} - x_{CO}^{out} > x_{CO_2}^{out} - x_{CO_2}^{in}$, otherwise Eq. (1b) was used:

$$X_{CO} = \frac{x_{CO}^{in} - x_{CO}^{out}}{x_{CO}^{in} \cdot (1 + x_{CO}^{out})} \tag{1a}$$

$$= \frac{x_{CO_2}^{out} - x_{CO_2}^{in}}{x_{CO}^{in} \cdot (1 - x_{CO_2}^{out})} \tag{1b}$$

2.3. Parameter estimation

From literature it is well-known that a power law fit can adequately describe the activity of the WGS reaction over broad ranges of temperature and composition for both CuZn-based [13] and FeCr-based catalysts [14]. This approach was also chosen for the noble-metal catalyst used here. The general form of this power law rate equation is:

$$R_{WGS} = k^0 \cdot e^{(-E_{a,i}/RT)} \cdot p_{H_2O}^{n_{H_2O}} \cdot p_{CO}^{n_{CO}} \cdot p_{CO_2}^{n_{CO_2}} \cdot p_{H_2}^{n_{H_2}} \cdot (1 - \beta) \tag{2}$$

where the term $(1 - \beta)$ represents the approach to equilibrium, written as:

$$1 - \beta = \left(1 - \frac{p_{CO_2} \cdot p_{H_2}}{p_{CO} \cdot p_{H_2O} \cdot K_{eq}}\right) \tag{3}$$

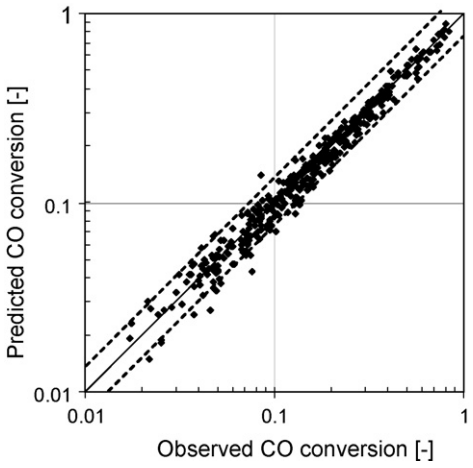

Fig. 1. Parity plot of the predicted versus the observed values for the CO conversion. Dashed lines represent a 25% deviation.

The equilibrium constant is obtained from the HSC thermodynamics software package and is expressed as:

$$K_{eq} = \frac{p_{CO_2} \cdot p_{H_2}}{p_{CO} \cdot p_{H_2O}} = \exp(Z(Z(0.563176 - 0.18210 \cdot Z) + 4.189249) + 0.341737) \tag{4}$$

with the reduced temperature factor Z defined as:

$$Z = \frac{1000}{T} - 1 \tag{5}$$

To reduce the correlation between the activation energy and the pre-exponential factor in the Arrhenius equations of the reaction rate coefficient, a reparameterization is applied:

$$k = k^0 \cdot e^{(-E_a/RT)} = e^{(k_{ref} + (E_a/RT_{ref})(1 - (T_{ref}/T))} \quad \text{with} \quad k_{ref} = \ln(k^0) - \frac{E_a}{RT_{ref}} \tag{6}$$

with 573 K chosen as the reference temperature.

Non-linear multi-response parameter estimation is performed using the GREGPLUS solver provided by the Athena Visual Workbench software [15]. Since at some settings high conversions of CO and/or H_2O occurred during the experiments, an isothermal 1D homogeneous integral reactor model was applied. The CO conversion is used as response parameter in the regression routine. Weight factors are introduced in the regression analysis to give every experimental data point an equal importance in the minimization procedure. These weight factors are the reciprocal values of the observed CO conversions, scaled to an average value of unity.

The parameter estimates are summarized in Table 2. The parity plot is presented in Fig. 1. The dashed lines in this figure represent a 25% deviation. A residual analysis gave no trends of the residuals with the parameter settings, indicating the absence of systematic errors within the model.

Although the WGS kinetics for noble-metal catalysts are not as frequently published as for the CuZn-based catalysts, e.g. [13] and

Table 2
Parameter estimates and according statistical parameters.

Parameter	Estimate	Estimated error (95% confidence interval)	Unit	t statistic
k^0	3.97E+05	±0.5E+05	mol kg^{-1} s^{-1} kPa$^{-0.21}$	−102
E_a	81.6E+03	±5E+03	J mol^{-1}	52
n_{H_2O}	0.72	± 0.04	–	31
n_{CO}	0.17	± 0.01	–	22
n_{CO_2}	−0.19	± 0.02	–	−15
n_{H_2}	−0.49	± 0.02	–	−37

FeCr-based catalysts, e.g. [14,16,17], the calculated reaction orders are in good agreement with the literature [18–20]. The reaction orders for the reactants are positive, CO having a weaker influence than H_2O. The reaction orders for the products are negative, CO_2 having a weaker influence than H_2.

3. WGS heat integration

3.1. Isothermal adiabatic concept

In adiabatic operation of a WGS reactor, the reaction rates are not optimized throughout the reactor. At reactor inlet the reaction rate is limited by the relatively low-temperature, while at reactor outlet the approach to thermodynamic equilibrium at higher temperature slows the net reaction rate. By proper heat management the overall reaction rate can be enhanced, leading to a lower requirement for catalyst mass.

Ideally, a profile with a decreasing temperature along the reactor length is forced in such a way that at every position in the reactor the reaction rate is maximized not being limited by a too low-temperature or a too near approach to equilibrium. In such a heat exchange WGS reactor more than a 2-fold reduction in catalyst mass compared to adiabatic operation is theoretically possible [21–23]. Although the optimal temperature profile is readily calculated, its implication is difficult to realize by means of a counter-current cooling medium. It involves careful tuning of the thermal conductivity of the solid phase. As a consequence, reactor design and operation is complex. Moreover, special measures have to be taken during start-up to ensure that the heat supplied by the entering reformate coming from the reformer is not taken-up directly by the exiting counter-current cooling medium at the reactor entrance. Without interruption of the cooling medium feed during start-up, this heat bypasses the reactor. This is characteristic for heat integrated reactors relying on heat transfer between two flows.

Alternatively to a decreasing temperature gradient, isothermal operation allows up to a 2-fold reduction of catalyst mass compared to adiabatic operation at identical conditions. For example, Pasel et al. [24] demonstrated that at isothermal operation higher CO conversions can be realized at lower gas inlet temperatures. Instead of using active heat exchange with a fluid, the present study uses the thermal conductivity of the catalyst support structure to obtain isothermal operation. By means of conduction, the reaction heat is distributed throughout the catalyst mass. For an exothermal reaction, this means that the reaction heat is transported upstream the catalyst bed. The temperature profile within the catalyst bed is levelled and the effective use of the catalyst is increased. Since no active heat exchange is applied, the adiabatic characteristic of the reactor is maintained. This concept is called isothermal adiabatic operation.

Assuming plug flow behavior, the pseudo-homogeneous, 1D energy and mass balances are written as:

$$W_s \cdot c_{p,s} \cdot \frac{\partial T}{\partial t} = -F_m \cdot c_{p,mol,g} \cdot \frac{\partial T}{\partial z} + \frac{A_{cross} \cdot \lambda_{eff}}{l} \cdot \frac{\partial^2 T}{\partial z^2} + W_{cat} \cdot \Delta_r H_{WGS} \cdot R_{WGS} \quad (7)$$

$$\frac{\partial C_i}{\partial t} = -\frac{1}{l}\frac{\partial (u_s \cdot C_i)}{\partial z} + \frac{\nu_i \cdot W_{cat}}{V_r} R_{WGS} \quad (8)$$

where z is the dimensionless bed length. The effective thermal conductivity λ_{eff} is essentially determined by the properties of the catalyst support structure, since the thermal conductivity of the gas is low. See the nomenclature for the other symbols. The following initial and boundary conditions apply:

$$t = 0 \forall z \quad C_i = C_i^{in};\ T = T^{in} \quad (9)$$

$$z = 0 \quad \frac{\partial (u_s \cdot C_i)}{\partial z} = 0;\ \frac{\partial T}{\partial z} = Pe_{th} \cdot (T - T^{in}) \quad (10)$$

$$z = 1 \quad \frac{\partial (u_s \cdot C_i)}{\partial z} = 0;\ \frac{\partial T}{\partial z} = 0 \quad (11)$$

The dimensionless energy balance is written as:

$$Le \cdot \frac{\partial T^*}{\partial \tau} = -\frac{\partial T^*}{\partial z} + \frac{1}{Pe_{th}} \cdot \frac{\partial^2 T^*}{\partial z^2} + Da_{th} \cdot R^*_{WGS} \quad (12)$$

where Le is the Lewis number, Pe_{th} the thermal Peclet number and Da_{th} the thermal Damköhler number [25,26]. The backwards transport of heat by conduction is promoted by decreasing the thermal Peclet number. This is illustrated in Fig. 2, where simulated temperature profiles for the WGS reaction throughout the catalyst bed are presented for different values for Pe_{th} and Da_{th}. For a given catalyst volume and feed flow rate (i.e. GHSV), lowering Pe_{th} can be done by increasing the effective thermal conductivity of the support, and/or by increasing the cross-sectional area and simultaneously decreasing the bed length. In the first simulation case in Fig. 2, the thermal conductivity is negligible, i.e. $Pe_{th} = \infty$. For packed beds Pe_{th} is typically 500 and the shift of the temperature profile is marginal. Even when significantly decreasing Pe_{th} to 50 its value is still too high for significant back conduction of heat. At a further decrease to 5 the effect becomes noticeable. Only for $Pe_{th} = 0.5$ or lower isothermal adiabatic operation is approached. Note that in this case the feed gas at the inlet of the reactor is instantaneously heated by 84 K from 533 K to 617 K while the catalyst bed has a small temperature difference of 7 K.

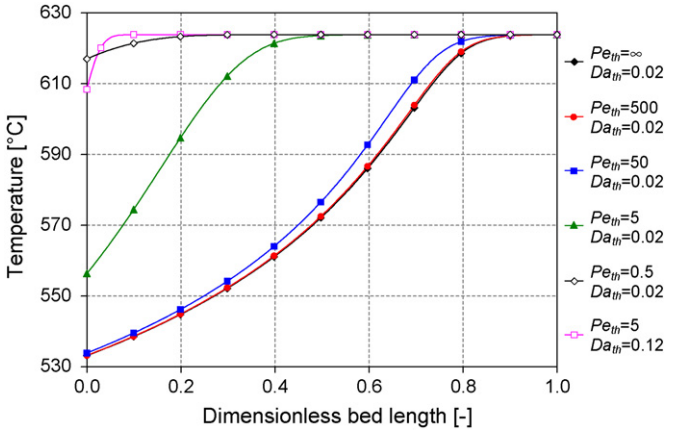

Fig. 2. Simulated temperature profiles throughout the reactor for varying values for Pe_{th} and Da_{th}. Feed conditions: $T_{gas,inlet}$ = 533 K, 8.7 vol.% CO, 7.7 vol.% CO_2, 28 vol.% H_2O, 25 vol.% H_2, balance N_2, F_v = 160 Nl min^{-1}, P = 150 kPa.

Furthermore, for limited values of Pe_{th} (e.g. $Pe_{th} = 5$) increasing the thermal Damköhler number from 0.02 to 0.12 stimulates the isothermal adiabatic operation. For a specific reaction and at fixed GHSV, this can only be achieved by increasing the catalyst activity. But of course increasing catalyst activity results in compacter reactors independent from the reactor concept. On the other hand, for a chemical reaction having a larger reaction heat than the WGS reaction, the thermal Damköhler number is larger and the isothermal adiabatic concept has a large potential to increase the efficient use of catalyst.

For the isothermal adiabatic concept, the heat is maintained within the reactor, meaning that heat does not bypass the reactor during the start-up as might be observed for heat exchanger designs discussed in the beginning of this paragraph. The start-up time of the isothermal adiabatic reactor, however, is somewhat larger

than for an adiabatic reactor because of the ideal mixing of the heat throughout the catalyst structure near catalyst light-off. This ideal mixing causes the heat produced by reaction to be partially transferred to the reactor outlet. In contrast, in the adiabatic reactor the heat production is mainly used locally to heat the thermal mass. At similar thermal mass, the start-up time for the isothermal adiabatic reactor is about 5 times longer than for the adiabatic reactor.

3.2. Isothermal adiabatic reactor design

For an experimental verification of the concept, two approaches were applied. First, an open-cell aluminum foam (ERG Materials and Aerospace Corporation, USA) with an effective thermal conductivity of 14 W m^{-1} K^{-1} was applied as catalyst support. It is manufactured via the indirect copying production technique; polymer foam is embedded in ceramic material from which the polymer foam is removed by heating to obtain a negative cast. Liquid aluminum is subsequently enforced into the negative mould resulting in a replicate of the original polymer foam structure [27]. In contrast to direct copying where the polymeric foam serves as the mould, indirect copying results in solid strands which favor thermal conductivity. Second, an aluminum metal monolith (Emitec, Germany) with an effective thermal conductivity of 32 W m^{-1} K^{-1} was applied. The aluminum metal monolith consisted of stacked layers of flat and corrugated sheets, rolled up and contained in an aluminum metal tube. See Table 2 for the specifications of both these catalyst structures. The dimensions correspond to the catalyst volume needed for the WGS section within a 5 kW$_e$ diesel fuel processor. Using autothermal reforming of diesel, the total reformate flow is about 175 Nl min^{-1} having a CO content between 7 vol.% and 9 vol.%.

The moderate effective thermal conductivity for the open-cell aluminum foam calls for a substantial cross-sectional area of the catalyst bed to reach a sufficiently low Pe_{th} value. Therefore, a radial-flow concept was applied to avoid an unpractical "pancake" reactor. The catalyst bed is annulus-shaped, with the gas flowing from the outside to the inside [28,29], conform the schematic in Table 2. Because of the low-pressure drop of the foam, the gas distribution within the foam structure is optimized by placing the annulus-shaped foam between cylindrical sintered metallic filter elements (GKN, Germany). The aluminum metal monolith having a higher effective conductivity allows for axial flow without resulting in a too shallow catalyst layer. Both the aluminum foam as the aluminum monolith were coated by Umicore with catalyst loadings similar to that applied for standard 400 cpsi cordierite monoliths. To measure the temperature distribution, nine thermocouples were positioned within each catalyst structure.

A cross-section of the coated aluminum monolith is shown in Fig. 3. While all flat sheets have a 5–10 μm thick coating, the catalyst coating is thicker at curvatures. In the hollow curvature of the corrugated sheets the coating thickness amounts to 60 μm. At the spots where the corrugated sheets contact the flat sheets, the catalyst coating is thickest at about 300 μm. The coating has a BET surface area of 75 m^2 g^{-1} and the porosity was measured to be 60%. It was verified numerically that no significant mass and heat transfer resistances are present within the coating [12]. While the coating of the foam was not analyzed in detail, visual inspection indicated that dip coating of such a large 3D structure resulted in a rather thick catalyst layer at the outer surface of the structure. On several spots, clusters of cells were even clogged by catalyst.

4. Results and discussion

The performance of the foam and of the monolith structure was verified by measuring the catalytic activity as a function of the gas

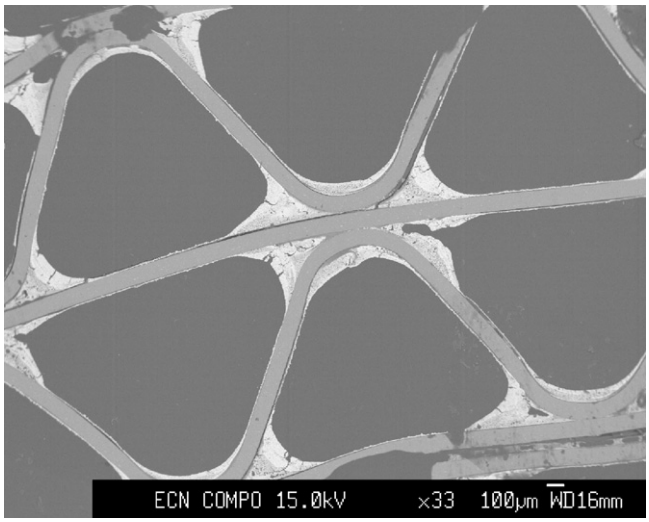

Fig. 3. Electron microscopic representation of the coated monolith.

inlet temperature. The gas temperature was increased from 473 K to 573 K at a rate of 1 K min^{-1} for the foam and 0.2 K min^{-1} for the monolith. For both catalyst structures this was done repeatedly to condition the catalyst.

The resulting activity plots for the foam catalyst and the monolith catalyst are presented in Figs. 4 and 5, respectively. The simulated activity plots for the adiabatic operation and the ideal isothermal adiabatic operation of these reactors are included. The simulations show an expected gradual catalyst light-off for the adiabatic reactors. At low inlet temperatures the simulations show only a moderate effect of the back mixing of heat for the isothermal adiabatic concept since the catalyst activity for the isothermal adiabatic reactor is only slightly higher than that of the adiabatic reactor. At a certain inlet temperature, however, the model predicts a steep catalyst light-off for the isothermal adiabatic reactors. This happens at 508 K for the foam catalyst and at 493 K for the monolith catalyst under the conditions specified in the captions of the figures. The CO conversion increases from 20% to its equilibrium value at an increase of the gas inlet temperature of only a few degrees. At the light-off temperature, the upstream conductive transport of the heat that is produced in the downstream part of the structure becomes effective in increasing the upstream catalyst temperature. This again invokes an increased upstream heat production and an increased upstream heat transport, resulting in a

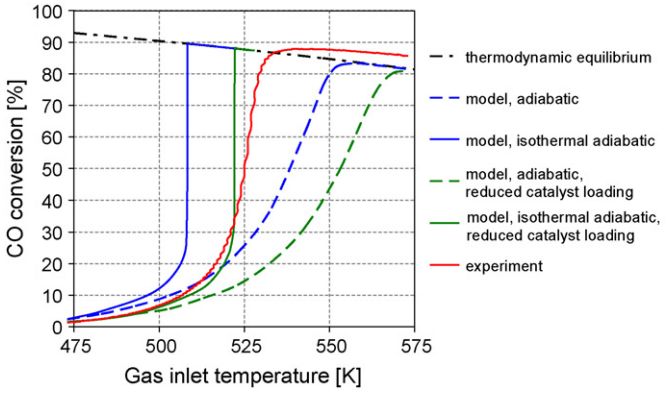

Fig. 4. Simulated and measured activity plot a function of the reactor inlet temperature for the foam reactor configuration. Feed conditions: 8.0 vol.% CO, 7.0 vol.% CO_2, 25 vol.% H_2O, 24 vol.% H_2, balance N_2, F_v = 175 Nl min^{-1}, P = 150 kPa, experimental ramp rate = 1 K min^{-1}.

flattened temperature profile throughout the whole catalyst structure. This steep catalyst light-off is typical of isothermal adiabatic operation.

The experimental activity plot (red line) for the foam catalyst in Fig. 4 is shifted towards a higher temperature compared to the corresponding calculated isothermal adiabatic activity plot (blue line) (For interpretation of the references to color in this text, the reader is referred to the web version of the article). Strikingly, the measured catalyst activity at low-temperature, i.e. at a temperature where the back mixing of heat is negligible, is much lower than simulated. Therefore, the simulations are repeated with a reduced catalyst loading to 65% (green lines). The measured performance in terms of the low-temperature activity and the catalyst light-off much better approaches this new simulation. This suggests that only about 65% of the catalyst present on the foam structure was utilized, in agreement with visual inspection of the foam coating. Next to the low availability of the catalyst, the steepness of the measured light-off is somewhat less pronounced compared to the simulations. Two effects partially explain this experimental result. First, the temperature ramp of 1 K min^{-1} is somewhat high at the point of light-off. As discussed in Section 3.1 the mixing of heat by conduction results in a larger thermal response time compared to adiabatic operation. Therefore, the measured activity does not represent the steady state activity. As will be shown for the monolith structure, a slower heating rate, e.g. 0.2 K min^{-1}, would have been more appropriate. Second, the axial temperature distribution within the catalyst structure was not homogeneous. A maximum temperature difference of 9 K was measured between the top and the bottom of the structure during light-off. This results from the radial-flow field applied. As can be seen in the schematic drawing of the flow field in Table 2, the relatively cold feed gas contacts the top of the foam structure creating a heat sink even after applying insulation. Nevertheless, the experiment clearly indicates that isothermal adiabatic operation can be approached by using the foam structure.

The experimental activity plot for the monolith catalyst is shown in Fig. 5. In this case, the measured activity as a function of the inlet temperature is much better predicted by the simulated curve for the isothermal adiabatic operation (blue solid line) (For interpretation of the references to color in this text, the reader is referred to the web version of the article). Illustratively, the measured maximum radial temperature difference is lower at about 3 K. The entire catalyst mass is used and the slower heating ramp of 0.2 K min^{-1} results in a sharper experimental catalyst light-off. Additional to the steady state curve for the isothermal adiabatic operation, the activity plot was also simulated applying a ramp of 0.2 K min^{-1}, represented by the solid black line. Inclusion of the heating rate

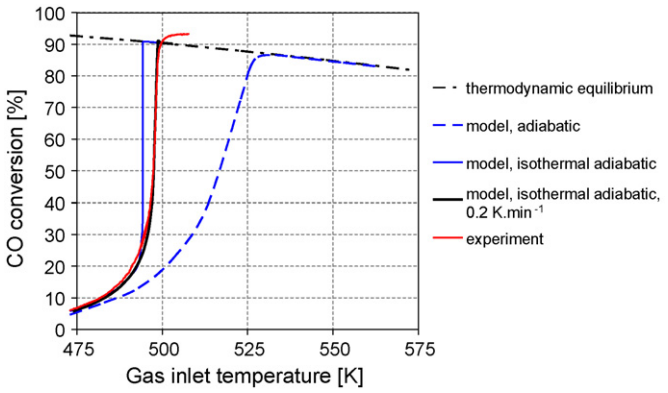

Fig. 5. Simulated and measured activity plot a function of the reactor inlet temperature for the monolith reactor configuration. Feed conditions: 8.7 vol.%CO, 7.7 vol.% CO_2, 28 vol.% H_2O, 25 vol.% H_2, balance N_2, F_v = 160 Nl min^{-1}, P = 150 kPa, experimental ramp rate = 0.2 K min^{-1}.

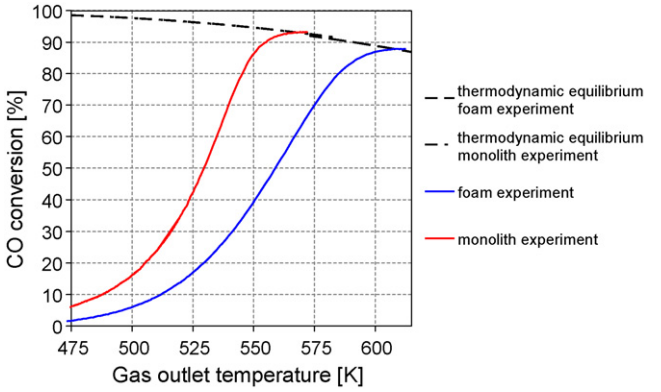

Fig. 6. Experimental activity as a function of the measured reactor outlet temperature for the foam and the monolith reactor configuration.

results in a slightly more gradual light-off, in good agreement with the measurement. For the foam structure, accounting for the even faster heating rate of 1 K min^{-1} in a similar way indeed partially explains the more gradual catalyst light-off observed experimentally in Fig. 4 (not shown). While simulating the activity plot using a temperature ramp rather than a steady state approach, the rates for heating of the thermal mass and the distribution of the heat by conduction are accounted for. As indicated in Section 3.1, the thermal conductivity causes these responses to be somewhat sluggish, resulting in a less steep catalyst light-off when using a temperature ramp. The results clearly evidence that isothermal adiabatic operation can be achieved by using a monolith structure.

In Figs. 4 and 5, for both the foam and the monolith structure, the measured CO conversion following catalyst light-off appears higher than expected thermodynamically. This is caused by a heat loss to the environment for the reactors. Illustratively, Fig. 6 shows the same experimental CO conversion as in the previous figures but plotted as a function of the measured reactor outlet temperature rather than the inlet temperature. It is observed that for both the foam and the monolith reactor, the measured conversion approaches the thermodynamic equilibrium line. Comparing the in- and outlet temperatures at maximum CO conversion indicates that about 15% of the reaction heat is lost for the foam catalyst, while about 30% of the reaction heat is lost for the monolith catalyst. The increased heat loss for the monolith catalyst directly results from the high thermal conductivity of the support. Besides axial flattening of the temperature profile, in radial direction it results in an increased heat flow to the reactor wall leading to a potentially larger heat loss [9,10].

Based on the presented results, further optimization of the monolith reactor should focus on increasing the thermal resistance between the aluminum monolith and the reactor wall by proper packing in order to minimize heat loss. Second, further compacting could be achieved by increasing the catalyst loading, by increasing the cell density of the monolith and by applying thicker aluminum sheets. These measures would increase the thermal Damköhler number and would allow a larger length–diameter ratio for the catalyst structure when maintaining the thermal Peclet number.

5. Implications for the isothermal adiabatic reactor concept

The experimental validation of the isothermal adiabatic reactor using the metal monolith catalyst support showed a reduction of the CO content from 8.7 vol.% to 0.6 vol.% in a single reactor. This CO level is sufficiently low for a subsequent CO polishing unit, being either a preferential oxidation reactor (PrOx) [30] or a methanation reactor [31]. The catalyst amount used in the isothermal

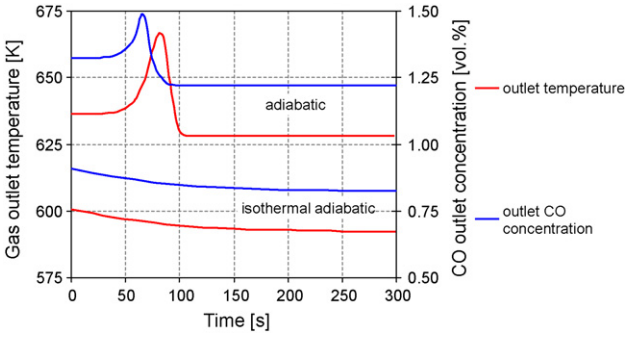

Fig. 7. Simulated open loop responses for the outlet temperature and the CO outlet concentration to a 10 K downward step change in inlet temperature for an adiabatic reactor (upper part of the figure) and an isothermal adiabatic reactor (lower part of the figure). Base case conditions: 8.7 vol.% CO, 7.7 vol.% CO_2, 28 vol.% H_2O, 25 vol.% H_2, balance N_2, F_v = 160 Nl min^{-1}, P = 150 kPa, $T_{gas,in}$ = 548 K for adiabatic reactor, $T_{gas,in}$ = 508 K for isothermal adiabatic reactor.

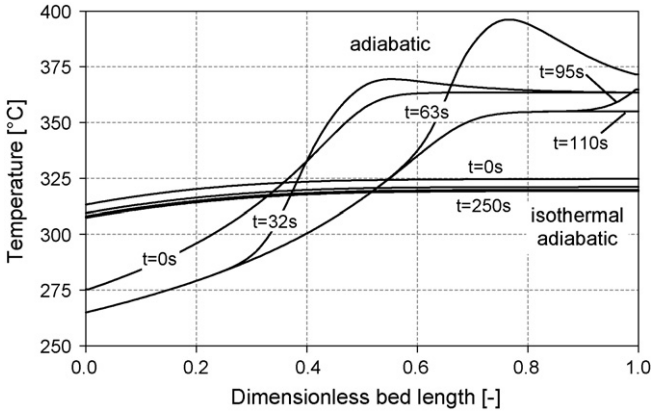

Fig. 9. Simulated axial temperature profiles of the adiabatic and the isothermal adiabatic reactor during the step down in inlet temperature. The settings are the same as in Fig. 7.

adiabatic reactor corresponds to the catalyst amount that would be needed in a double staged adiabatic WGS unit, reducing the CO content from 8.7 vol.% to 0.3 vol.%. Using the Umicore catalyst on cordierite honeycombs for both stages, they are operated at $GHSV_{WGS1}$ = 30,000 h^{-1} ($WHSV_{WGS1}$ = 153 Nm^3 kg^{-1} h^{-1}) and $GHSV_{WGS2}$ = 20,000 h^{-1} ($WHSV_{WGS2}$ = 96 Nm^3 kg^{-1} h^{-1}), respectively This implies that a single WGS reactor based on the isothermal adiabatic concept using an aluminum metal monolith operating at GHSV = 11,000 h^{-1} ($WHSV_{WGS1}$ = 55 Nm^3 kg^{-1} h^{-1}) can replace a double staged adiabatic WGS section with interstage heat exchanger at a small decrease in the overall CO conversion. This significantly simplifies the fuel processor layout.

Besides this favorable steady state behavior, the dynamic behavior is also important from system point of view. In this respect, the simulated open loop responses of an isothermal adiabatic reactor and an adiabatic reactor are compared. In Fig. 7a 10 K step down is simulated, i.e. 508–498 K for the isothermal adiabatic reactor and 548–538 K for the adiabatic reactor. In Fig. 8 a step up in feed flow from 160 Nl min^{-1} to 180 Nl min^{-1} is simulated. These perturbations are considered realistic events in a fuel processor. Fast feed flow changes could result from load changes. Fast feed temperature changes could result upon small changes of the steam-to-carbon or the oxygen-to-carbon ratios for an autothermal reformer. In the simulations, the perturbations take place at t = 0, at which point the reactors are at steady state, i.e. fully developed concentration and temperature profiles. The upper part of the figures represents the responses for the temperature and the CO concentration at the outlet of the adiabatic reactor, while the lower part of the figures represents those for the isothermal adiabatic reactor.

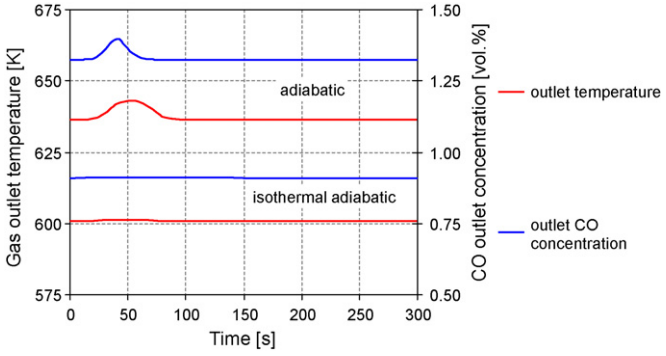

Fig. 8. Simulated open loop responses for the outlet temperature and the CO outlet concentration to an 20 Nl min^{-1} upward step change in feed flow for an adiabatic reactor (upper part of the figure) and an isothermal adiabatic reactor (lower part of the figure). Base case conditions: 8.7 vol.% CO, 7.7 vol.% CO_2, 28 vol.% H_2O, 25 vol.% H_2, balance N_2, F_v = 160 Nl min^{-1}, P = 150 kPa, $T_{gas,in}$ = 548 K for adiabatic reactor, $T_{gas,in}$ = 508 K for isothermal adiabatic reactor.

For the adiabatic reactor a step down in inlet temperature causes the outlet temperature and the outlet CO concentration to display inverse responses before the steady state values are achieved, see Fig. 7. The changes towards the new steady state are slower, but more gradual for the isothermal adiabatic reactor. For the adiabatic reactor, a decrease in inlet temperature causes the reaction rate at the upstream part of the bed to drop. The associated lower conversion causes high CO concentrations to enter the hotter downstream part of the bed, where the local steady state is thus disturbed. These higher CO concentrations result in a locally increased CO conversion and associated heat production in the downstream part of the bed. Although the perturbation is a decrease in feed temperature, the first response is an increase in outlet temperature and CO concentration. Following this inverse response, the outlet temperature and CO concentration go towards their new steady state values. The thermal wave progressing through the adiabatic reactor is compared with the temperature profiles for the isothermal adiabatic reactor in Fig. 9. The increase in CO associated to this inverse response amounts to 1600 ppm. For the isothermal adiabatic reactor, such a wave is absent because of the flat axial temperature profile and high thermal conductivity. The high thermal conductivity causes the whole axial temperature profile to gradually change into the new steady state profile.

A step up in feed flow (load) causes the outlet temperature and outlet CO concentration to increase for the adiabatic reactor, while no significant changes in the responses are observed for the isothermal adiabatic reactor, see Fig. 8. For the adiabatic reactor, increasing the load causes the axial steady state concentration profiles to be pushed downstream, while the temperature profile reacts slower because of the thermal mass associated with the catalyst and its support. The local steady state is disturbed in the sense that high CO concentrations are transported downstream to the hotter part of the bed. Similarly to the temperature step down case, the CO conversion increases locally and again an increased outlet temperature and CO outlet concentration result. At these specific conditions the associated increase in CO amounts to 700 ppm. For the isothermal adiabatic reactor, such a wave in temperature and CO concentration along the reactor axis is not present because of the flat axial temperature profile and the high thermal conductivity of the catalyst structure. Pushing the concentration profiles downstream thus not result in a locally higher heat production.

Although not shown here, additional simulations verified that step changes in the feed composition give similar results: large inverse responses for the adiabatic reactor while changes in the outlet temperature and composition for the isothermal adiabatic reactor are smooth. A fast change in, e.g. the steam content could result from a change in quench flow between the reformer and the WGS section. These simulations illustrate that the isothermal adiabatic approach results in a more robust reactor operation compared to adiabatic reactors. The simulated temporary increase in CO outlet concentration for the adiabatic reactor influences the performance of the downstream CO polishing units. This may result in a temporary increase in CO content of the PEMFC feed. The isothermal adiabatic reactor concept significantly reduces these unwanted temporary increases. Accordingly, the PrO*x* section can be operated at a lower air surplus and more stable operation of a downstream methanation section or PSA would result. Moreover, elaborate control schemes, such as model predictive control, that are applied for adiabatic reactors to minimize the effect of thermal waves travelling through the reactor [26,32,33] would not be required for the isothermal adiabatic concept. Instead a much simpler control of the reactor inlet temperature only can be applied, meaning that efficient control of the upstream heat exchanger would suffice.

It must be noted, however, that the isothermal adiabatic concept is very sensitive to a temperature drop below the catalyst light-off temperature. As discussed in Section 4, below this critical temperature the heat production is too low to ensure effective heat distribution by conduction and the conversion readily drops.

6. Conclusions

The concept of isothermal adiabatic operation of the WGS reactor for a fuel processor was demonstrated. By increasing the back mixing of the reaction heat throughout a continuous catalyst structure, the catalyst bed is nearly isothermal while the adiabatic character is maintained. Accordingly, a very steep catalyst light-off is observed for the isothermal adiabatic concept at a much lower feed temperature than for an adiabatic reactor. Based on measured intrinsic kinetics, reactors were designed for both aluminum metal foam and aluminum metal monolith supported catalysts. The reaction kinetics could adequately be described by a power law rate equation. Although catalyst coating of the foam appeared troublesome due to its large 3D structure, the performance of the monolith reactor agreed very well the model predictions. This single stage isothermal adiabatic reactor replaces the conventional double staged adiabatic operation with intermediate heat exchange. Besides the favorable steady state performance, simulations show the robustness of the isothermal adiabatic concept in dynamic operation. Compared to the conventional adiabatic reactors, this would allow significantly simpler process control and leads to a lower risk for the PEMFC feed to experience temporary increased CO contents.

Acknowledgement

Dr. Matthias Duisberg from Umicore AG & Co. KG, Hanau, Germany, is gratefully acknowledged for the fruitful discussions, for providing the catalysts and for characterization of the catalyst coating.

References

[1] J. Agrell, H. Birgersson, M. Boutonnet, I. Melián-Cabrera, R.M. Navarro, J.L.G. Fierro, Production of hydrogen from methanol over Cu/ZnO catalysts promoted by ZrO_2 and Al_2O_3, J. Catal. 219 (2003) 389–403.
[2] D.L. Trimm, Minimisation of carbon monoxide in a hydrogen stream for fuel cell application, Appl. Catal. A: Gen. 296 (2005) 1–11.
[3] A. Qi, B. Peppley, K. Karan, Integrated fuel processors for fuel cell application: a review, Fuel Process. Technol. 88 (2007) 3–22.
[4] C. Ratnasamy, J.P. Wagner, Water–gas shift catalysis, Catal. Rev. 51 (2009) 325–440.
[5] A.S. Quiney, G. Germani, Y. Schuurman, Optimization of a water–gas shift reactor over a Pt/ceria/alumina monolith, J. Power Sources 160 (2006) 1163–1169.
[6] D.G. Norton, E.D. Wetzel, D.G. Vlachos, Thermal management in catalytic microreactors, Ind. Eng. Chem. Res. 45 (1) (2006) 76–84.
[7] G. Kolb, J. Schürer, D. Tiemann, M. Wichert, R. Zapf, V. Hessel, H. Löwe, Fuel processing in integrated micro-structured heat-exchanger reactors, J. Power Sources 171 (2007) 198–204.
[8] A. Moreno, K. Murphy, B.A. Wilhite, Parametric study of solid-phase axial heat conduction in thermally integrated microchannel networks, Ind. Eng. Chem. Res. 47 (23) (2008) 9040–9054.
[9] G. Groppi, E. Tronconi, Design of novel monolith catalyst supports for gas/solid reactions with heat exchange, Chem. Eng. Sci. 55 (1–2) (2000) 2161–2171.
[10] E. Tronconi, G. Groppi, T. Boger, A. Heibel, Monolithic catalysts with 'high conductivity' honeycomb supports for gas/solid exothermic reactions: characterization of the heat-transfer properties, Chem. Eng. Sci. 59 (22–23) (2004) 4941–4949.
[11] D.C. Montgomery, Design and Analysis of Experiments, 6th ed., John Wiley and Sons, New York, 2005.
[12] G.F. Froment, K.B. Bischoff, Chemical Reactor Analysis and Design, 2nd ed., Wiley Series in Chemical Engineering, New York, 1990.
[13] J.L. Ayastuy, M.A. Gutiérrez-Ortiz, J.A. González-Marcos, A. Aranzabal, J.R. González-Velasco, Kinetics of the low-temperature WGS reaction over a $CuO/ZnO/Al_2O_3$ catalyst, Ind. Eng. Chem. Res. 44 (1) (2005) 41–50.
[14] H. Bohlbro, The kinetics of the water–gas conversion at atmospheric pressure, Acta Chem. Scand. 15 (1961) 502–520.
[15] Athena Visual Studio, http://www.athenavisual.com.
[16] H. Bohlbro, The kinetics of the water–gas conversion II investigations at elevated pressures, Acta Chem. Scand. 16 (1962) 431–438.
[17] H. Bohlbro, The kinetics of the water–gas conversion III influence of H_2S on the rate equation, Acta Chem. Scand. 17 (1963) 1001–1011.
[18] G. Germani, P. Alphonse, M. Courty, Y. Schuurman, C. Mirodatos, Platinum/ceria/aluminium catalysts on microstructures for carbon monoxide conversion, Catal. Today 110 (2005) 114–120.
[19] S. Hilaire, X. Wang, T. Luo, R.J. Gorte, J. Wagner, A comparative study of water–gas-shift reaction over ceria-supported metallic catalysts, Appl. Catal. A: Gen. 258 (2004) 271–276.
[20] R. Radhakrishnan, R.R. Willigan, Z. Dardas, T.H. Vanderspurt, Water–gas shift activity and kinetics of Pt/Re catalysts supported on ceria–zirconia oxides, Appl. Catal. B: Environ. 66 (2006) 23–28.
[21] J.M. Zalca, D.G. Löffler, Fuel processing for PEM fuel cells: transport and kinetic issues of system design, J. Power Sources 111 (2002) 58–64.
[22] W.E. TeGrotenhuis, D.L. King, K.P. Brooks, B.J. Golladay, R.S. Wegeng, Optimizing microchannel reactors by trading-off equilibrium and reaction kinetics through temperature management, in: 6th International Conference on Microreaction Technology, 2002.
[23] E.V. Rebrov, S.A. Kuznetsov, M.H.J.M. de Croon, J.C. Schouten, Study of the water–gas shift reaction on Mo_2C/Mo catalytic coatings for application in microstructured fuel processors, Catal. Today 125 (1–2) (2007) 88–96.
[24] J. Pasel, R.C. Samsun, D. Schmitt, R. Peters, D. Stolten, Test of a water–gas-shift reactor on a 3 kWe-scale – design points for high- and low-temperature shift reaction, J. Power Sources 152 (2005) 189–195.
[25] N.H. Bell, T.F. Edgar, Modelling of a fixed bed water–gas shift reactor. 1. Steady state model verification, J. Process Contr. 1 (1991) 22–31.
[26] G.T. Wright, T.F. Edgar, Nonlinear model predictive control of a fixed bed water–gas shift reactor: an experimental study, Comput. Chem. Eng. 18 (2) (1994) 83–102.
[27] J. Banhart, Manufacture, characterisation and application of cellular metals and metal foams, Prog. Mater. Sci. 46 (2001) 559–632.
[28] C.S. Yoo, A.G. Dixon, Maldistribution in the radial-flow fixed bed reactor, NATO ASI Series, Series E 110 Chemical Reactor Design and Technology, in: H.I. De Lasa (Ed.), Proc. of ASI, London/Ontario, Canada, 1985, pp. 838. ISBN: 90-247-3315-4, NIJHOFF (Chem. React. Des. Technol.) (1986) 749–757.
[29] H.C. Chang, M. Saucier, J.M. Calo, Design criteria for radial flow fixed bed reactors, AIChE J. 29 (6) (2004) 1039–1041.
[30] S.H. Oh, R.M. Sinkevitch, Carbon monoxide removal from hydrogen-rich fuel cell feedstreams by selective catalytic oxidation, J. Catal. 142 (1993) 254–262.
[31] P. Panagiotopoulou, D.I. Kondarides, X.E. Verykios, Selective methanation of CO over supported noble metal catalysts: effects of the nature of the metallic phase on catalytic performance, Appl. Catal. A: Gen. 344 (2008) 45–54.
[32] S.T. Lin, Y.H. Chen, C.C. Yua, Y.C. Liu, C.H. Lee, Dynamic modeling and control structure design of an experimental fuel processor, Int. J. Hydrogen Energy 31 (2006) 413–426.
[33] W. Mitchell, B.J. Bowers, C. Garnier, F. Boudjemaa, Dynamic behavior of gasoline fuel cell electric vehicles, J. Power Sources 154 (2006) 489–496.